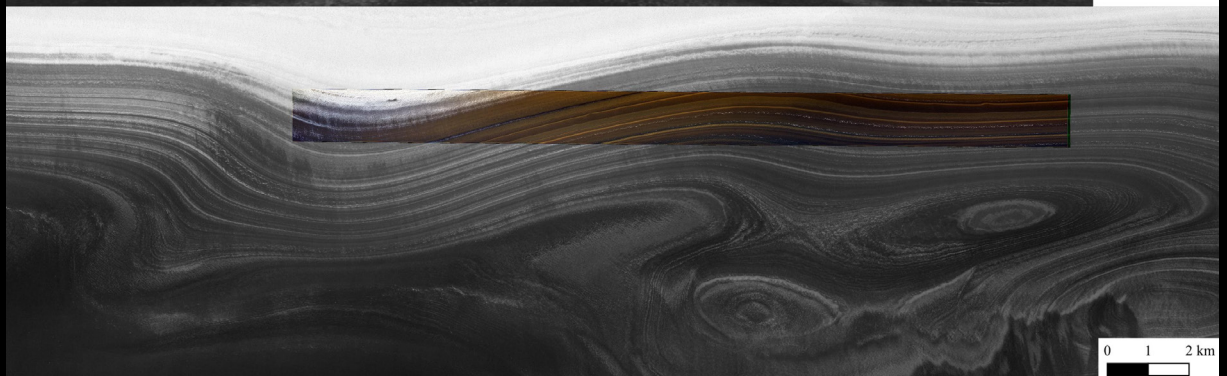
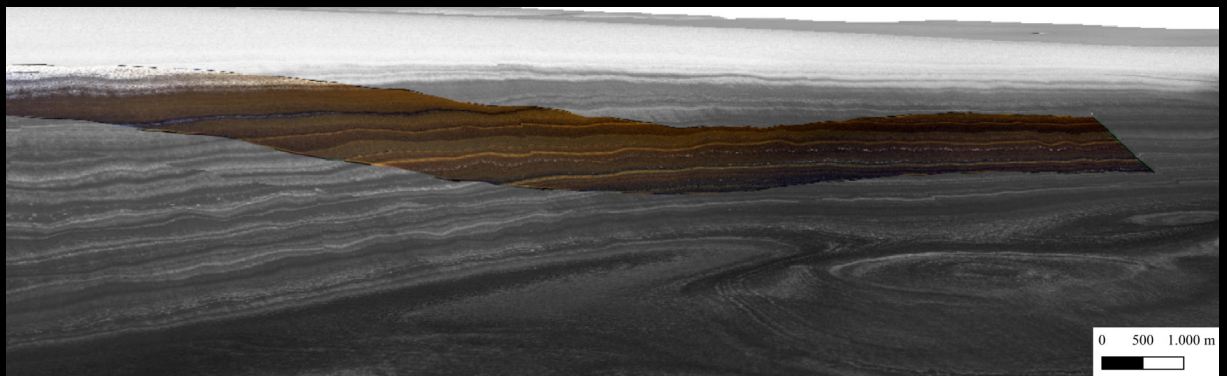


Geological *Field Trips* and *Maps*



SOCIETÀ GEOLOGICA ITALIANA

FONDATA NEL 1867 - ENTE MORALE R. D. 17 OTTOBRE 1885



 **ISPRA**
Istituto Superiore per la Protezione
e la Ricerca Ambientale



Sistema Nazionale
per la Protezione
dell'Ambiente

Geological map of the Nord Rupes (North Polar Cap, Mars)

<https://doi.org/10.3301/GFT.2024.04>

2024

Vol. 16 (1.4)



ISSN: 2038-4947

GFT&M - *Geological Field Trips and Maps*

Periodico semestrale del Servizio Geologico d'Italia - ISPRA e della Società Geologica Italiana
Geol. F. Trips Maps, Vol.16 No.1.4 (2024), 17 pp., 7 figs., 4 tab., 4 eq. (<https://doi.org/10.3301/GFT.2024.04>)

Geological map of the Nord Rupes (North Polar Cap, Mars)

**Nicole Costa¹, Matteo Massironi^{1,3}, Luca Penasa², Sabrina Ferrari¹,
Riccardo Pozzobon^{1,3} & Jacopo Nava¹**

¹ Dipartimento di Geoscienze, Università degli Studi di Padova, Via Gradenigo 6, 35131 Padova (PD), Italy.

² Osservatorio Astronomico di Padova (OAPD), Istituto Nazionale di Astrofisica (INAF), Vicolo dell'Osservatorio 5, 35122 Padova (PD), Italy.

³ Centro di Ateneo di Studi e Attività Spaziali "Giuseppe Colombo" (CISAS), Università degli Studi di Padova, Via Venezia 15, 35131 Padova (PD), Italy.

Corresponding author e-mail: nicole.costa@studenti.unipd.it

Responsible Director
Marco Amanti (ISPRA-Roma)

Editor in Chief
Andrea Zanchi (Università Milano-Bicocca)

Editorial Manager
Angelo Cipriani (ISPRA-Roma) - *Silvana Falchetti* (ISPRA-Roma)
Fabio Massimo Petti (Società Geologica Italiana - Roma) - *Diego Pieruccioni* (ISPRA - Roma) - *Alessandro Zuccari* (Società Geologica Italiana - Roma)

Associate Editors
S. Fabbi (Sapienza Università di Roma), *M. Berti* (Università di Bologna),
M. Della Seta (Sapienza Università di Roma), *P. Gianolla* (Università di Ferrara),
G. Giordano (Università Roma Tre), *M. Massironi* (Università di Padova),
M.L. Pampaloni (ISPRA-Roma), *M. Pantaloni* (ISPRA-Roma),
M. Scambelluri (Università di Genova), *S. Tavani* (Università di Napoli Federico II)

Editorial Advisory Board
D. Bernoulli, *F. Calamita*, *W. Cavazza*, *F.L. Chiocci*, *R. Compagnoni*,
D. Cosentino, *S. Critelli*, *G.V. Dal Piaz*, *P. Di Stefano*, *C. Doglioni*, *E. Erba*,
R. Fantoni, *M. Marino*, *M. Mellini*, *S. Milli*, *E. Chiarini*, *V. Pascucci*, *L. Passeri*,
A. Peccerillo, *L. Pomar*, *P. Ronchi*, *L.*, *Simone*, *I. Spalla*, *L.H. Tanner*,
C. Venturini, *G. Zuffa*

Technical Advisory Board for Geological Maps
F. Capotorti (ISPRA-Roma), *F. Papasodaro* (ISPRA-Roma),
S. Grossi (ISPRA-Roma), *M. Zucali* (University of Milano),
S. Zanchetta (University of Milano-Bicocca),
M. Tropeano (University of Bari), *R. Bonomo* (ISPRA-Roma)

Cover page Figure:

3D and 2D view of the Nord Rupes, Mars, made by HiRISE colour image and CTX image on the MOLA DEM.

ISSN: 2038-4947 [online]

<http://gftm.socgeol.it/>

The Geological Survey of Italy, the Società Geologica Italiana and the Editorial group are not responsible for the ideas, opinions and contents of the guides published; the Authors of each paper are responsible for the ideas, opinions and contents published.

Il Servizio Geologico d'Italia, la Società Geologica Italiana e il Gruppo editoriale non sono responsabili delle opinioni espresse e delle affermazioni pubblicate nella guida; l'Autore/i è/sono il/i solo/i responsabile/i.

INDEX

Introduction	4	Geological mapping	11
Previous regional stratigraphic works	4	Water ice unit	12
Study area	5	Dusty water ice unit	12
Data and methods	6	Pure and dusty dry ice group	12
Data-set	6	Undifferentiated ice-dominated bedrock	13
Methods and software	6	Surficial units	13
Results	7	Stratigraphic column and geological sections	13
Spectral analysis	7	Conclusions	13
		References	16

ABSTRACT

The geology of Martian Polar Caps provides details about depositional rates of dust and ices correlated with the present or past climate of the planet. Up to date, the North polar dome has been studied mainly at regional scale using spectral and radar data, but detailed stratigraphic studies are still very limited and, in any case, not coupled with geological maps.

At the edge of the Martian North Polar Cap (86°N 233°E) a 500 m-high upwind scarp between Boreales Scopuli and Olympia Rupes well exposes the upper sequences of the North Polar Layered Deposits (NPLD*) revealing a layered and laterally continuous sequence of icy and dusty strata.

Using CRISM, SHARAD, CTX and HiRISE* data, we recognised and mapped several geological units along the scarp and interpreted their morphological, spectral and stratigraphic characters. In addition, SHARAD radargrams were employed to correlate radar reflectors in the subsurface with the outcropping geological units and, consequently, to produce the geological sections complementing the geologic map (scale 1: 70.000). This approach demonstrated for the first time that the surficial composition and stratigraphy of the NPLD valley can accurately match the variation in radar backscatter of subsurface radargrams.

*see acronym table (Tab.4) at the end of the manuscript.

Keywords: Mars, North Polar Cap, Olympia Planum, Stratigraphy, Radargrams.

INTRODUCTION

The North Polar Cap on Mars is made up mostly of water ice, ice of carbon dioxide and silicate dust, distributed in different amount within the stratigraphic sequence of the so called “North Polar Layered Deposits (NPLD; e.g., Ojha et al., 2019). Polar deposits are indeed stratified in alternated bright and dark layers, shaped by ancient climate fluctuations conditioned by orbital parameters (Phillips et al., 2008; Becerra et al., 2017; Milkovich et al., 2008).

The flatness of the strata reflects the flat-shaped dome morphology of the ice deposits (Byrne, 2009; Putzig et al., 2009) which are carved by troughs (or valleys) tens of metres to kilometres deep. They are formed and enlarged by the aeolian erosion of katabatic winds, that blow perpendicularly with respect to the steep edge of the North cap and are driven westward by the Coriolis force. Those winds accelerate downslope, erode the equator-facing scarp exposing the stratified series and deposit the aeolian sediments upslopes on the pole-facing slope (Masse et al., 2012). The ice flowing from the central point of the cap towards the margins contributes to generate the troughs (Zuber et al., 1998; Tanaka et al., 2008), which spirally cut the polar cap (Milkovich et al., 2008) and create counter-clockwise spirals in anti-Coriolis direction. Layers exposed along polar outcrops are formed by relatively young deposits estimated to span from ~3.6 My to ~8.7 Ky (Latest Amazonian; Byrne, 2009; Tanaka et al., 2008) with a high

uncertainty in age estimation (e.g., Phillips et al., 2008; Milkovich et al., 2008; Becerra et al., 2017).

The main goal of this paper is to map the layered deposits exposed along a 500-m steep slope, named Nord Rupes, facing the Olympia Planum and, following Mirino et al. (2018) procedure, correlate their composition and stratigraphy with the subsurface radar reflectors, using the data acquired by the NASA Mars Reconnaissance Orbiter instruments. In particular, we performed (a) a surface stratigraphic and morphological interpretation using high-resolution panchromatic images and hyperspectral data, and (b) a subsurface reconstruction based on radar-reflectors. Our results underline that the radar-based stratigraphy can be directly related to the stratigraphic record recognisable at the surface, including its spectral variability.

PREVIOUS REGIONAL STRATIGRAPHIC WORKS

The North Polar Cap is important for climatic studies, as its stratigraphy provides a record of the past climatic conditions on the planet. The polar cap is made up of a) 2 km-thick, layered and generally laterally continuous sequence of strata called North Polar Layered Deposits (NPLD) with diverse albedo reflecting a variable amount of water ice and lithic inclusions (Byrne, 2009); and at the bottom by b) 1 km-thick, non-continuous, darker, layered Basal Unit (BU) composed of weakly cemented basaltic sandstone and possibly evaporites (Putzig et al., 2009). The whole polar cap is piled up over an Early-Amazonian broad plain with polygonal troughs, ghost craters and subdued wrinkle ridges known as Vastitas Borealis Formation (VBF; Tanaka et al., 2008).

In Tanaka et al. (2008), NPLD and BU are subdivided into further specific sub-units by means of morphological and compositional interpretation of data from different missions and instruments (e.g., OMEGA from Mars Express, THEMIS from Mars Odyssey and MOC from Mars Global Surveyor). In particular, authors defined the well-stratified sequence made up of layers with different albedo and ice/dust content as “Planum Boreum units”. These are alternated with badly-stratified units that show variable nature, for example poorly or highly consolidated, fractured or discontinuous layers of ice-cemented gypsum or dark weathered basalts (Tanaka et al., 2008).

The Shallow Radar (SHARAD)-based stratigraphy proposed by Putzig et al. (2009) identifies different units on the basis of the pattern of radar reflections in the radargrams. Units are packet-inter-packet sequences with variable thickness, radar reflectance and flatness/horizontality (Putzig et al., 2009). They are linked to the units previously defined. In particular, radar units A and B correspond to VBF and BU, respectively, while the NPLD can be associated with the radar units C, D, E, F and G.

STUDY AREA

Many scarps that expose layers could be found along the polar troughs, especially close to the edge of the polar cap. We focused our attention on an East-West trending valley (Fig. 1) located on the North-Western cap edge facing Olympia Planum. According to Mars Orbiter Laser Altimeter (MOLA) data, the Nord Rupes is characterised by 140

km of length and 20 km of maximum width. The exposed stratigraphy on the equator-facing scarp belongs to (Fig. 1): a) the upper part of the dome-shaped sequence defined as radar-unit G by Putzig et al. (2009); b) the uppermost 2 km-thick part of the NPLD (Byrne, 2009); c) Planum Boreum units 1 and 3 of Tanaka et al. (2008). Planum Boreum 1 unit is made up of hundreds of sub-horizontal and m-thick layers with different albedo due to the variable composition of ice

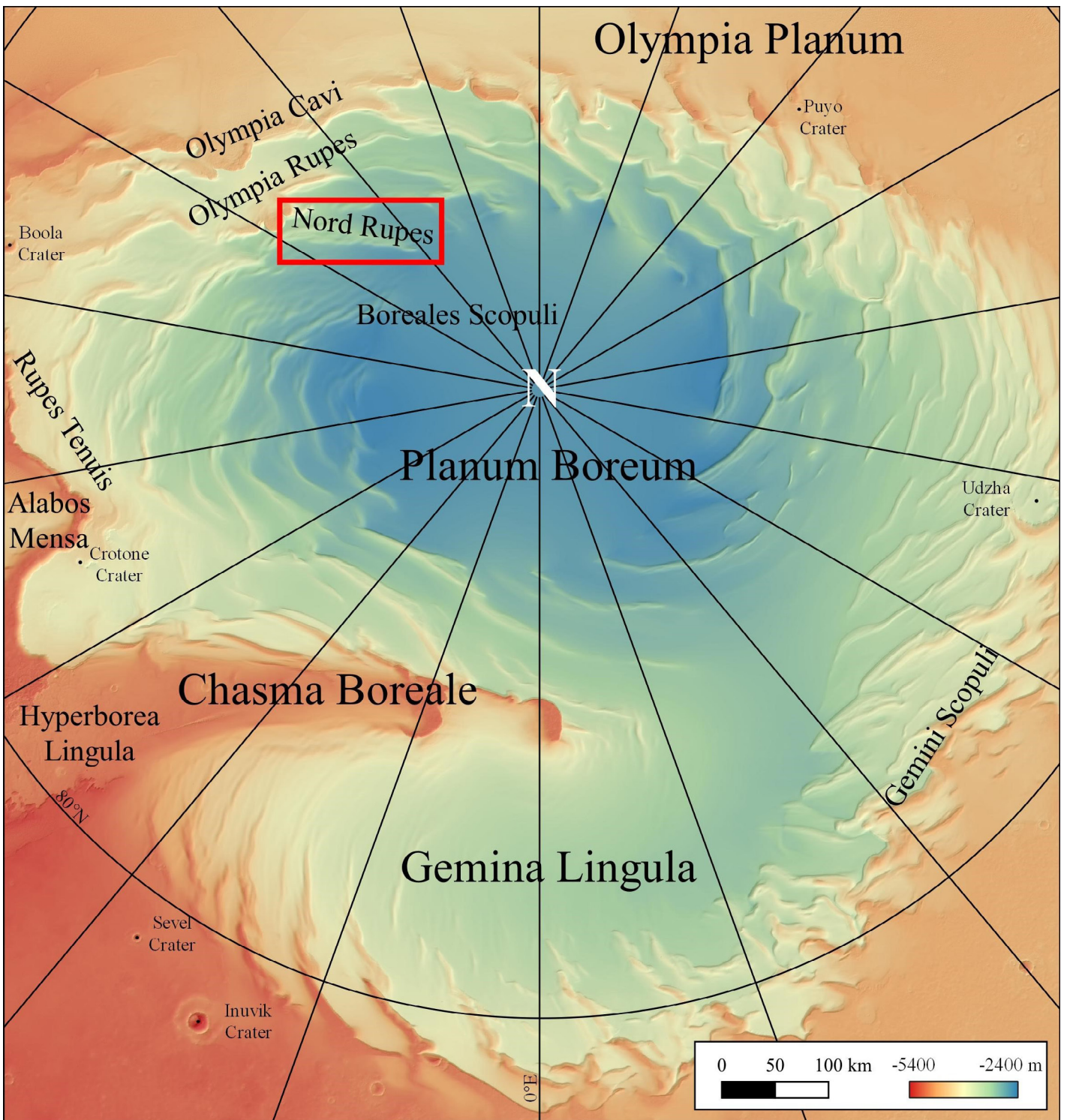


Fig. 1 - Topographic map of the Martian North Polar Cap (based on MOLA DEM) with studied valley highlighted by the red rectangle.

and dust and dates back to the Middle to Late Amazonian. It includes some erosional local unconformities and surficial features like pits, ridges, brecciated material and aeolian yardangs. The unit is covered by Planum Boreum 3 unit of the Late Amazonian, featuring 6-8 poorly-defined tens of metres-thick layers of moderate content in pure H₂O ice and some percentage of dust (Tanaka et al., 2008). Polar Boreum 2 unit is not exposed at the tops of equator-facing rupes (e.g., Nord Rupes) because eroded or not deposited in these locations (Tanaka et al., 2008).

Despite the interest in the polar regions, no detailed geological maps of the polar cap have been produced up to date. Some geological maps are published of the whole polar body or at regional scale (e.g., Skinner and Herkenhoff, 2012; Tanaka et al., 2008), but they represent only wide units that can hide stratigraphic details crucial for deciphering the climate-NPLD relationship.

DATA AND METHODS

Data-set

We used data from both the cameras onboard the NASA Mars Reconnaissance Orbiter, the Context Camera (CTX) and the High Resolution Imaging Science Experiment (HiRISE). CTX images have a spatial resolution of 6 m/px and cover an area of 30 x 160 km (Malin et al., 2007; Zurek and Smrekar, 2007). CTX contextualizes the HiRISE images, which have a spatial resolution of 25 cm/px and cover an area of 6 x 12 km (McEwen et al., 2007; Zurek and Smrekar, 2007). From the same space mission, we also used data from the Compact Reconnaissance Imaging Spectrometer for Mars (CRISM), which acquires hyperspectral cubes in the 362-3920 nm spectral wavelength range with a spectral resolution of 6.55 nm and a spatial resolution of 18-36 m/px (Murchie et al., 2007; Zurek et al., 2007; Viviano-Beck et al., 2014; Seelos et al., 2019). Finally we used Shallow

Radar (SHARAD) radargrams (distance on x-axis and time on y-axis), which have a vertical resolution of 10 m in free space and <1 km subsurface penetration (Seu et al., 2007; Zurek et al., 2007), and the Mars Orbiter Laser Altimeter (MOLA; Smith et al., 2001) digital elevation model (DEM), which gave us topographic information with spatial resolution of 115 m/px. All data used for this work (see Tab. 1) were downloaded from NASA PDS Geosciences Node Mars Orbital Data Explorer (ODE; <https://ode.rsl.wustl.edu/mars/>). In particular, we used CTX Experiment Data Record (EDR) images, HiRISE Reduced Data Record (RDR) images, CRISM Map-projected Targeted Reduced Data Record (MTRDR) hyperspectral cubes and SHARAD Reduced Data Record of Radar backscatter power (USRDR) radargrams. Moreover, the SHARAD USRDR radargrams has been compared with SHARAD Clutter Simulation in order to verify what we have mapped.

Methods and software

We chose a polar scarp where CRISM cube shows a certain spectral variability and the camera sensors a large number of exposed layers. We also identified four equally spaced and NNW-SSE oriented SHARAD radargrams, to provide a cross-sectional view of the subsurface arrangement of the outcropping layers (Tab. 1). Radar data would indeed show the same layering intercepted by the slopes at the surface. All optical data were thus imported in open-source QGIS software, where they are co-registered using the “Raster Georeferencer” tool and projected according to GCS Mars 2000 coordinate system and polar stereographic projection. We first distinguished six units on the base of morphological and reflectance variations on CRISM image: (i) surficial sediments; interleaving alternation of dark and light layers subdivided in an (ii) upper and a (iii) lower part on the base of their overall albedo; (iv) dark layered materials; (v) non-layered materials and (vi) unclassified materials (Fig. 2). We decided to analyze spectrally only a limited area of the

Table 1 - List of data used in this work.

Instrument	Type of datum	Name of datum	Spatial resolution	Other information
CTX	Image	J02_045407_2661_XN_86N127W	6 m/px	Covered area: 30x160 km
CRISM	Hyperspectral cube	HRL0000c002_07_if185j_mtr3	18-36 m/px	Spectral resolution: 6.55 nm
HiRISE	Image	psp_010357_2660_red esp_045407_2660_red	25 cm/px	Covered area: 6x12 km
SHARAD	Radargram	r_0414302_001_ss05_700_a_lbl_c0l r_4896301_001_ss19_700_a_lbl_c0l r_1444102_001_ss19_700_a_lbl_c0l r_3503801_001_ss11_700_a_lbl_c0l	10 m (vertical)	subsurface penetration: <1 km
MOLA	DEM	megt__n_512_1_DEM	115 m	

stratified scarp (units i, ii, iii and iv) in order to minimize the photometric alterations due to the variable topography and the aberrations at the margin of the CRISM hyperspectral imaging data.

We imported in ENVI the CRISM hyperspectral cube, which was however affected by supersaturation in the range between 2650 and 2800 nm and heavy striping above 2800 nm (Carter et al., 2012). Therefore, our analysis was limited to bands up to 2650 nm. We identified five units in the CRISM image (called A, B, C, D and E in Fig. 2) and for each of them extracted their representative spectra of the scarp stratification using specific Regions of Interest (ROIs) of ~50 pixels each. Mean spectra of the five ROIs were smoothed by the Savitzky-Golay method with a 10 points of windows (Fig. 3; Luo et al., 2005). The five ROIs are within units that, according to Tanaka et al. (2008), are characterised by a mixture of CO₂ and water ices and possible basaltic dust at a different relative amount. Band depths were calculated on significant absorption bands (Fig. 4a-b, Tab. 2 and Eq. 1; Clark, 1999). The mean spectra of the five ROIs were used as reference for a Spectral Angle Mapper (SAM) classification, which is characteristically unaffected by illumination and albedo conditions and helped us identifying the different units throughout the CRISM subset (Fig. 4c; Kruse et al., 1993).

We also produced standard spectral indexes images following Viviano-Beck et al. (2014) using the ENVI plugin CRISM Analysis Toolkit (CAT; available from PDS Geoscience Node; Bultel et al., 2013) applied on the entire CRISM image. This dataset enabled us to discriminate layer stacks of different composition across the scarp (Fig. 5). False-color images were created from original CRISM data by selecting three bands of characteristic absorption peaks or using the spectral indexes selected for specific classes

of minerals (H₂O and CO₂ ices, iron-oxides and Fe-bearing minerals; Fig. 6). The obtained images were then imported in QGIS software, where they were subjected to pan-sharpening process.

We integrated these data with CTX and HiRISE images to define geological units and subunits identified on the basis of their texture, layering, morphology, color, reflectance and stratigraphic correlation, using the QGIS plugin Mappy (PLANMAP-GMAP project; Penasa et al., 2020). The resulting geological map mapped at the scale of 1:25000 is presented at the scale of 1:100000 (see attached map). Finally, subsurface interpretation of the polar cap was based on SHARAD radargrams, which have y-axis expressed in arrival time. The y-axis in depth was obtained by using the altitudes in metres derived by the topographic sections extracted from MOLA data along the SHARAD footpaths. The map-derived contacts were then projected into the topographic section by using the QGIS plugin qProf and software Inkscape and the related radar reflectors identified (Fig. 7).

RESULTS

Spectral analysis

The ROIs-derived signatures A and B, which correspond to the top of the scarps and the most surficial layers, are well distinguishable, whereas C, D and E, which have been collected in the middle and at the bottom of the scarp and the floor of the valley, respectively, have similar trend and thus analogous composition. We identified water ice thanks to characteristic absorption bands at 1020, 1240, 1500, 2000 and 2600 nm (Fig. 3; Seelos et al., 2019). In particular,

Table 2 - Parameters of calculated band depths for clays on blue spectrum A and for Fe-bearing (hydro-)oxides basing on green spectrum D.

Absorption bands	Expression component	Position of band	Band wavelength (nm)	CRISM band
Clays (2300nm)	B1	Center	2350.87	277
	B2	Left shoulder	2258.27	263
	B3	Right shoulder	2529.51	304
Fe-bearing (hydro-)oxides	B1	Center	520.72	14
	B2	Left shoulder	436.13	1
	B3	Right shoulder	592.35	25

Eq. 1: Expression used to calculate band depth for clays and Fe-bearing (hydro-)oxides (Clark and Roush, 1984).

$$BD = 1 - \left(\frac{B1}{\frac{B2 + B3}{2}} \right)$$

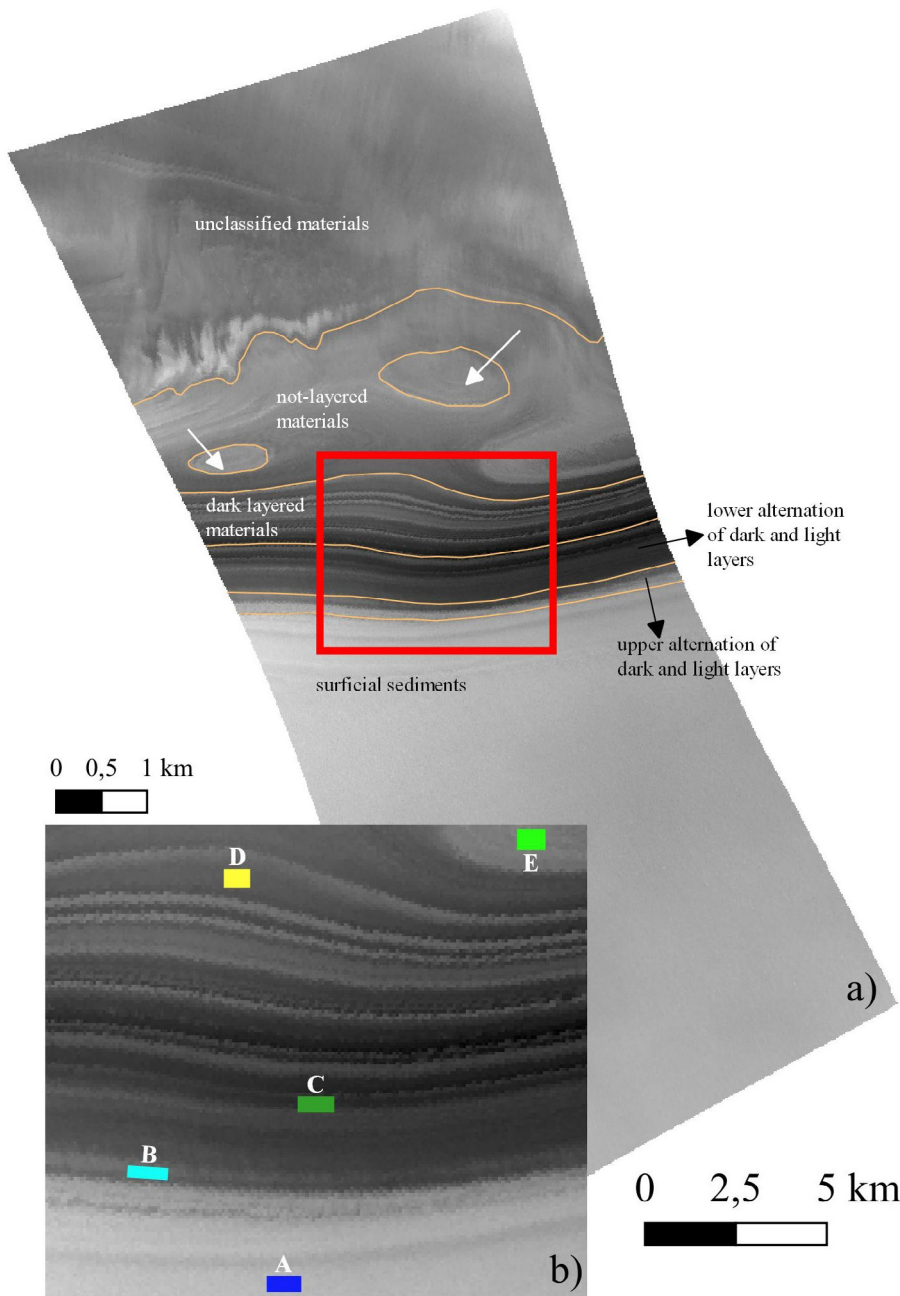


Fig. 2 - a) CRISM image with six-unit boundaries on the base of morphological and albedo variations. The limited position of the image objective of a more detailed spectral analyses is shown with a red rectangle. The two small areas (see white arrows) belong to the unit called “dark layered materials”; b) Detail of CRISM data, where the five selected ROIs are shown.

spectrum A (blue color, Fig. 3) shows deep absorption bands associated to icy water, therefore layers of this region seem to be composed of relatively pure water ice with low quantity of dusty materials. CO₂ ice presents absorption peaks located around 2300 nm and 2600 nm (overlapped by other bands) and multiple peaks within the range 1950-2100 nm (Seelos et al., 2019): CO₂ ice absorption bands are well visible in spectra C (sea green), D (green) and E (yellow, Fig. 3) where H₂O peaks are shallower and narrower indicating a decrease in water content. However, in those spectra the characteristic CO₂ absorption at 1435 nm is always masked by the 1500 nm peak of water ice. The dry ice band at 2600 nm is also hidden by the absorption of icy water located at the same wavelength. Spectrum B (cyan;

Fig. 3), which should contain an intermediate amount of water ice, seems to be transitional between spectrum A and the endmember represented by spectra C, D and E. Spectra C, D and E should differ in the amount of dusty material. In general, fine dusty materials show mild absorption bands and they contribute to the aggregate spectrum by reducing the band depths of ices.

In all the signatures presented in the work, absorption minima located at 500, 780, 800, 900 nm can be caused by crystal field effects or charge transfer of iron of feric minerals and their alterations products, (hydro-)oxides or clays, since they are coupled with the absorption at 2300 nm. In particular, the absorption peak at ~2300 nm, visible especially in spectra A and B, is typical of Me/Fe-bearing

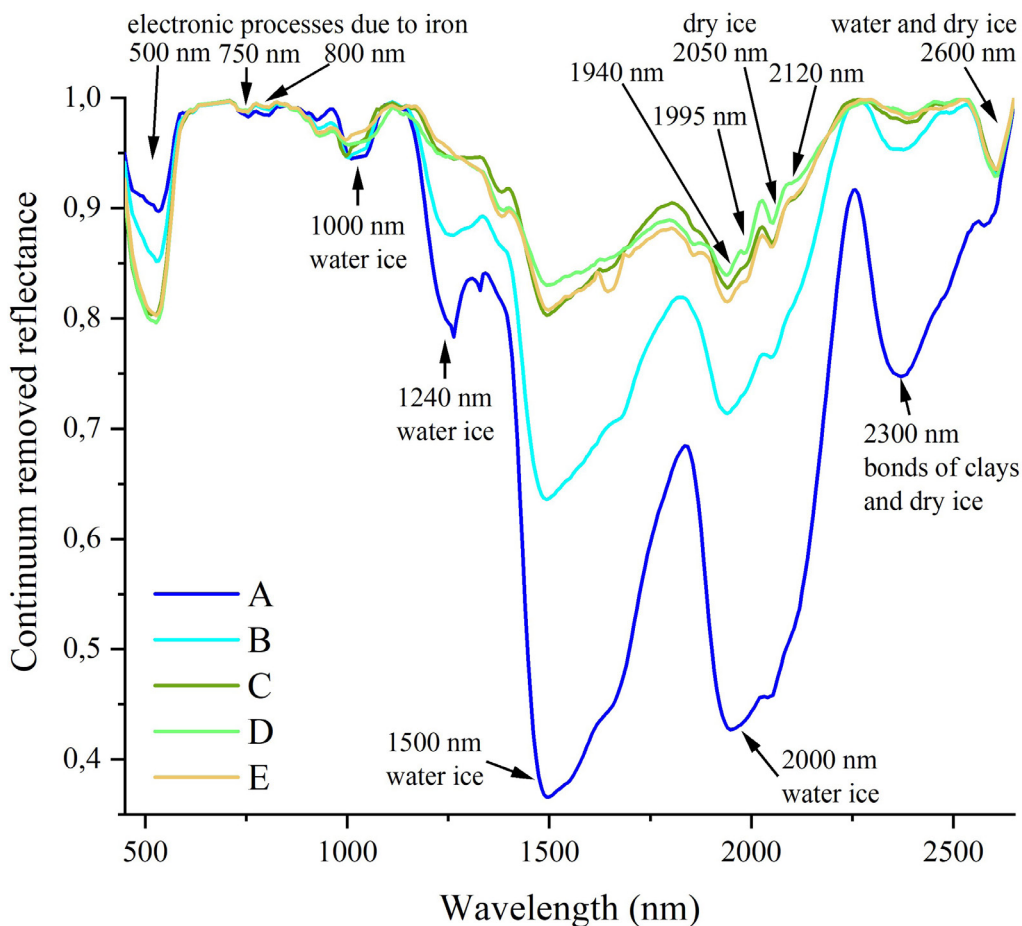


Fig. 3 - Plot of five mean spectra obtained by ROIs shown in Fig. 2b: each color line represents a ROI spectrum. Continuum is removed.

clays/phylosilicates (Seelos et al., 2019) derived from low-temperature aqueous alteration of feric minerals (Huang et al., 2017). Other distinctive features are not visible because they are overlapped by icy water absorption bands. This makes the spectral characterisation difficult.

We analysed the band depth of clays at 2300 nm, corresponding to Mg/Fe-OH bonds. The result shown in Fig. 4a indicates higher content of Fe-Mg bearing phyllosilicates (purple/fuchsia color) where greater amount of icy water is revealed by spectral signatures (spectra A and B, Fig. 3). Instead, the part showing different pink colors reveals alternating strata with variable, but still low, relative content of clays. We executed the second band depth at 500 nm to reveal the presence of Mg/Fe-bearing oxides and hydroxides, likely derived from alteration of basaltic dust (Tanaka et al., 2008). Fig. 4b displays higher content of Fe-bearing minerals in purple color and lower content in white. Hence the region with dry ice features in spectral signature (spectra C, D and E, Fig. 3) records higher amount of feric dust.

In Fig. 4c is shown the classification output of the SAM (taking 5 ROI spectra as reference) where all the classes have distinct boundaries indicating four main sectors: the lower part of the images (blue) is related to spectrum A, the two in-betweens (cyan and sea green) related to spectra B

and C and the upper part of the image is related to spectra D and E, which show a clear alternation. All the units are linked to the albedo variations and reflectance units of Fig. 2 as shown in Tab. 3.

Starting from previous results, which confirm the presence of water and dry ice, hydrated minerals and Fe-bearing dust, we identified appropriate indexes from Viviano-Beck et al. (2014) list to compositionally describe the whole detected area: a) BD1500_2 index based on Eq. 2 highlights the variable abundance of icy water, which is higher in the lower part of the images (Fig. 5a); b) BD_1435 index based on Eq. 3 aims at enhancing the absorption peak at 1435 nm of the CO₂ ice, which is concentrated in the upper part of the image (Fig. 5b); c) BD1900 index based on Eq. 4 detects the molecular bound of H₂O characteristic of hydrates minerals; d) RBR index based on slope between 440 and 770 nm wavelength ranges detects the presence of nanophase iron oxides. Indeed, feric mineral tends to become nanophase Fe-oxides because of space weathering, which extracts iron from feric minerals (Weber et al., 2022). Fe-bearing dust appears to be mostly focused on the upper part of the image similarly to BD1435 index indicating the presence of dry ice. Nevertheless, on the equator-facing scarp there is an alternation of bright and dark strata indicating a possible cyclical variability of iron oxides (Fig. 5c). A similar

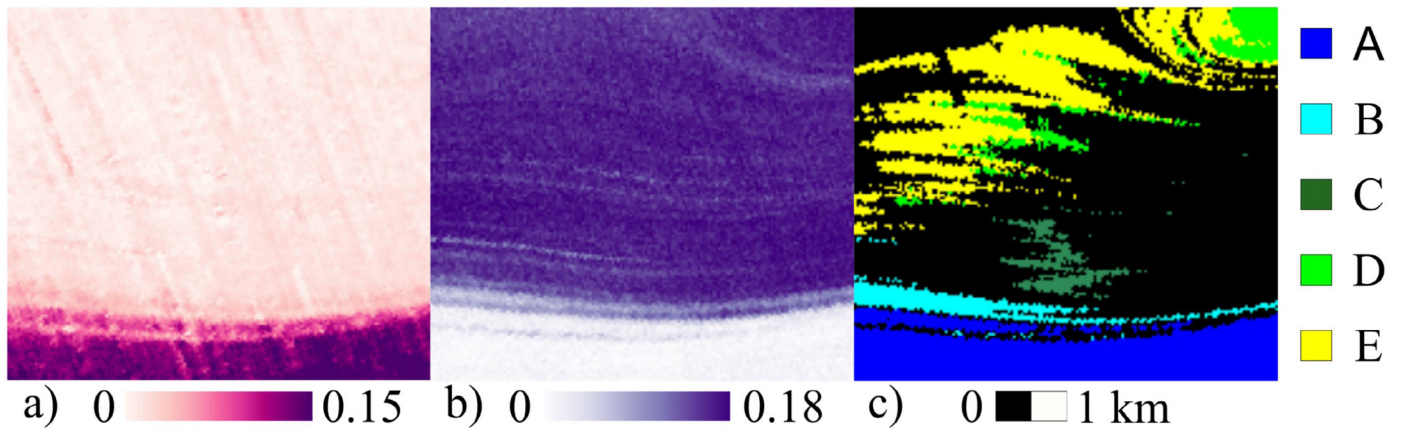


Fig. 4 - a) Results of band depth performed at 2300 nm: dark purple/fuchsia color indicates major absorption depths corresponding to major clay content, while pink indicates minimum absorption corresponding to minimum clay content; b) Results of band depth performed at 500 nm: purple color indicates major depth and Fe-bearing oxides and hydroxides content, contrariwise white color indicates minimum absorption and content of Fe-oxides. The position of the five ROIs are shown; c) Spectral Angle Mapper output on the study area: blue color is related to spectrum A and indicates region with the high presence of water ice, cyan color is related to the intermediate spectrum B which indicates a mixture of water ice and Fe-bearing minerals and sea green, green and yellow colors are related to spectrum C, D and E respectively and indicate variable mixture of dry ice and dust in addition to icy water.

Table 3 - Correlation between all (sub-)units and classes contained in this work.

Tanaka et al. (2008) stratigraphy	Putzig et al. (2009) stratigraphy	Albedo and morphological units	SAM classes/ spectra	Geological units	Geological subunits	
Planum Boreum 3	G	surficial sediments	spectrum A	water ice (WI)	water ice (WI)	
Planum Boreum 1		alternation of dark and light layers (upper)	spectrum B	dusty water ice (WD)	dusty water ice top (WD1)	dusty water ice bottom (WD2)
		alternation of dark and light layers (lower)	spectrum C	dusty dry ice (DD)	dark dusty dry ice 1 (DD1)	dark dusty dry ice 2 (DD2)
					dusty dry ice 3 (DD3)	dusty dry ice 4 (DD4)
		dark layered materials	spectrum D	dry ice (DI)	dusty dry ice 5 (DD5)	dusty dry ice 6 (DD6)
					dry ice 1 (DI1)	dry ice 2 (DI2)
dry ice 3 (DI3)	dry ice 4 (DI4)					
not-layered material	spectrum E	dry ice 5 (DI5)				
not present	not present	unclassified materials	not present	undifferentiated ice-bedrock (UB)	undifferentiated ice-dominated bedrock (UB)	
				surficial	aeolian mantling deposits (ad)	
					floor-valley deposits (vd)	
					gravitational mass movements and deposits (gd)	
					scarp talus deposits (td)	

Eq. 2: Equation for band depth at 1500 nm to calculate BD1500₂ index, which detects the amount of icy water. R1525, R1367 and R1808 are the reflectance of the wavelengths at the center, at the beginning and at the end of the absorption band (Viviano-Beck et al., 2014).

$$BD1500_2 = 1 - \left(\frac{R1525}{a * R1367 + b * R1808} \right)$$

Eq. 3: Equation for band depth at 1435 nm to calculate BD1435 index, which detects the amount of carbon dioxide ice, R1435, R1370 and R1470 are the reflectance of the wavelengths at the center, at the beginning and at the end of the absorption band (Viviano-Beck et al., 2014).

$$BD1435 = 1 - \left(\frac{R1435}{a * R1370 + b * R1470} \right)$$

Eq. 4: Equation for band depth at 1900 nm to calculate BD1900_2 index, which detects the amount of hydrate minerals. R1930, R1985, R1850 and R2067 are the reflectance of the wavelengths at the center, at the beginning and at the end of the absorption band (Viviano-Beck et al., 2014).

$$BD1900_2 = 0.5 * \left(1 - \frac{R1930}{a * R1850 + b * R2067} \right) + 0.5 * \left(\frac{R1985}{a * R1850 + b * R2067} \right)$$

distribution is also shown by BDI1000VIS index obtained by integrated band depth in the spectral range of 833-1023 nm and representing regions where feric and Fe-bearing minerals and glass are abundant (Fig. 5d).

We used the TRU-color CRISM image (R=R600, G=R530, B=R440; Fig. 6a) which emulates true colors of the Martian surface and false color images based on the spectral indexes described above to carry out the image interpretation and geological mapping. In particular, ICE (R=BD1900_2, G=BD1500_2, B=BD1435; Fig. 6b) shows hydrated silicates in red and yellow colors; both BDI1000VIS_BD15002_BD1435 (R=BDI1000VIS=Fe-bearing materials, G=BD1500_2=H₂O, B=BD1435=CO₂; Fig. 6c) and RBR_BD15002_BD1435 (R=RBR=Fe-oxides, G=BD1500_2=H₂O, B=BD1435=CO₂; Fig. 6d) RGB images show the variation of Fe-bearing mineral contents among

layers being the low albedo bluish strata of relative pure CO₂ ice and the high albedo purplish ones of CO₂ ice mixed with Fe-bearing dust layers.

Geological mapping

On the base of the compositional information described in the previous section and the fine stratigraphy recognisable in the HiRISE data, twenty-two subunits grouped into five major units of the NPLD are mapped and extended to a more regional view using CTX data. In addition, using HiRISE and CTX data for geomorphological interpretation, aeolian and gravitational deposits are also distinguished (see attached map). Units and subunits are named according to their inferred dominant composition and described from the top to the bottom of the scarp.

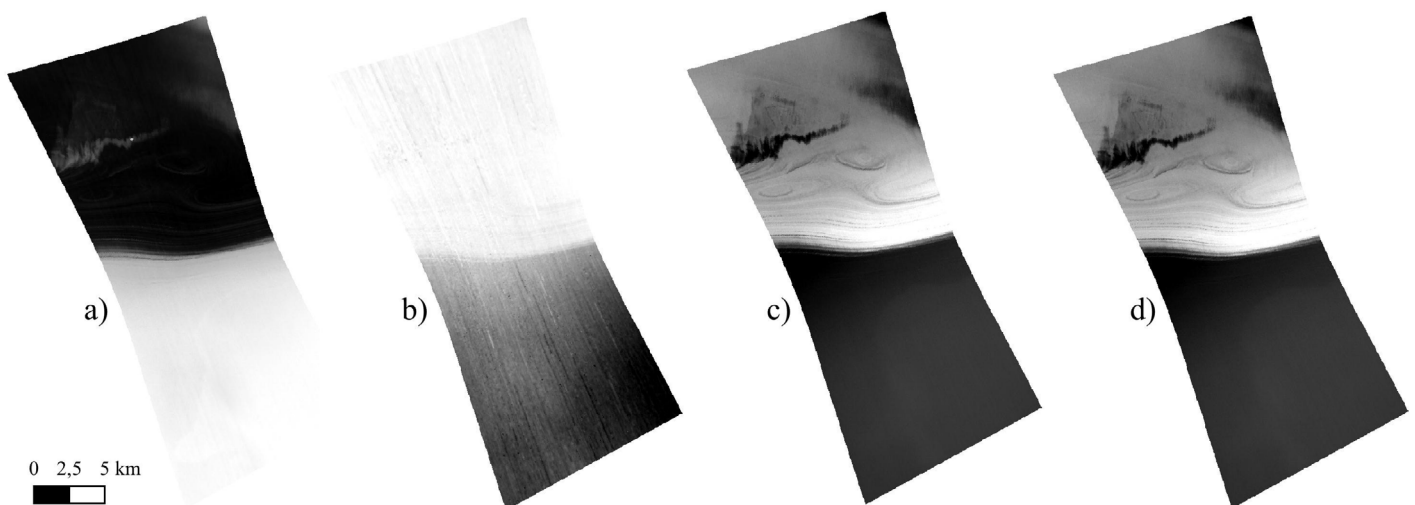


Fig. 5 - (a) BD1500_2 index displays water ice distribution; (b) BD1435 index displays dry ice distribution; (c) RBR index displays nanophase iron-oxides distribution; (d) BDI1000VIS index displays the distribution of Fe-bearing glass and minerals.

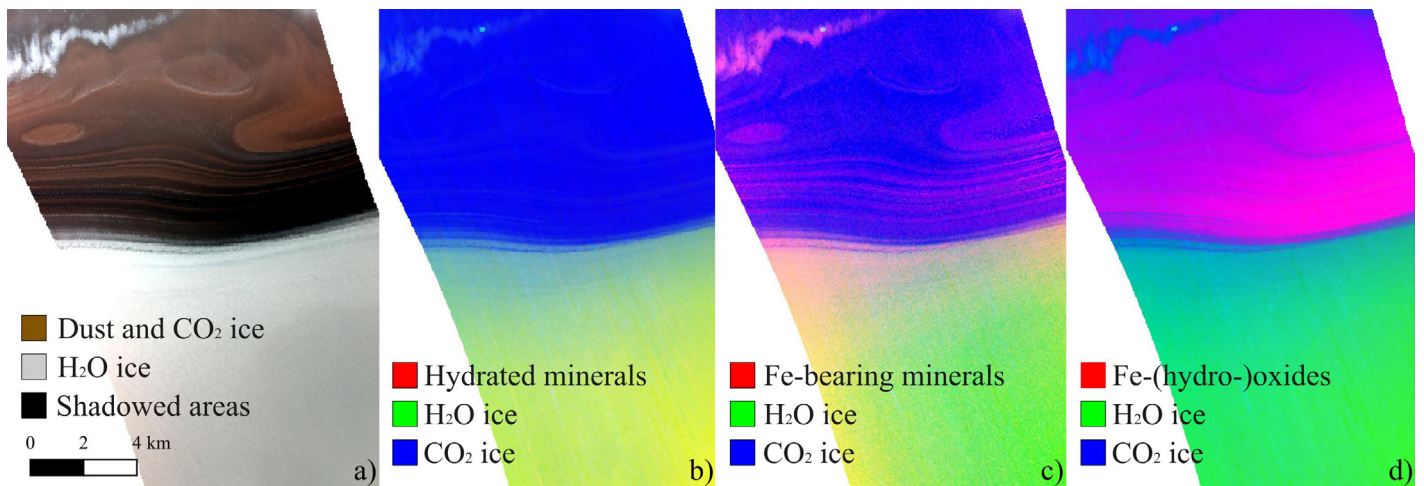


Fig. 6 - a) TRU image imitating the true surface colors; **b)** ICE image on which H₂O and CO₂ ices (green and blue colors respectively) and hydrated minerals (red colors) are detectable; **c)** BDI1000VIS_BD15002_BD1435 for the detection of ices (green and blue colors) and Fe-bearing minerals and glass (red color); **d)** RBR_BD15002_BD1435 to see ices (green and blue colors) and iron (hydro-)oxides (red colors).

Water ice unit

The *water ice unit* (WI; Fig. 7) is the uppermost flat unit, located at the top of the series along the equator-facing and pole-facing scarps. Its surficial extension is the largest among all units, the texture is smooth and the albedo is high in optical images (Fig. 2). It is mainly composed of relatively pure icy water and displays a white color in TRU image (Fig. 6a). The composition is supported by deeper absorption bands at 1500 and 2000 nm in the spectral signature A (Figs. 2-3-4 and Tab. 3) and confirmed by green colors in BDI1000VIS_BD15002_BD1435 and RBR_BD15002_BD1435 RGB images (Fig. 6b-c). On the top of the pole-facing scarp, this unit is covered by dry ice and dust mantling.

Dusty water ice unit

Under the water ice unit, the *dusty water ice unit* (WD) is identified by the presence of shallower water ice absorption bands with respect to previous unit, a limited increase of dry ice content and the presence of absorption bands related to feric oxides (see attached map), as shown by spectrum B (Fig. 3). It is constituted by two independent subunits also recognised by the radargram analysis (see Section 3.3). The *top subunit* (WD1) is made up of bright layers, where pure water ice is still the major component, and rare low-albedo strata enriched in dust. The *bottom subunit* (WD2) is a sequence constituted of same number of high and low-albedo layers. Here, the darkish color is more intense because of the possible higher amount of feric material (Fig. 6c-d).

Pure and dusty dry ice group

The underlying group is an alternation of layers richer in dry ice with different content of dust. DI1000VIS_

BD15002_BD1435 and RBR_BD15002_BD1435 RGB images highlight a sequence of bluish CO₂ and purplish dusty CO₂ layers (Fig. 6c-d). For simplification we split the group into *dry ice unit* (DI) and *dusty dry ice unit* (DD), both grouped together with strata of similar composition and features. The whole group has a total thickness of ~500 m and each layer never exceeds a decameter. Spectra C, D and E show double and multiple absorption peaks characteristic of CO₂ ice. Absorption bands of water ice are still present, but shallower if compared to the previous two units; Fe-bearing materials are also present. These three spectra are quite similar except for some absorption band depths and the general reflectance. Comparing BDI1000VIS_BD15002_BD1435 with RBR_BD15002_BD1435 indexes we were able to attribute spectrum E and the related yellow class in the SAM product (Figs. 2-3-4 and Tab. 3) to the bluish layers which are relatively rich in pure dry ice (Fig. 6c-d). For this reason, we denominated this unit *dry ice unit* (DI), which is also characterised by a low albedo in camera images (Fig. 2) and a dark color in the TRU image (Fig. 6a). All six layered subunits that we found are without specific features: *dry ice 1* (DI1), *dry ice 2* (DI2), *dry ice 3* (DI3; the only one ending laterally in a pinch-out structure), *dry ice 4* (DI4) and *dry ice 5* (DI5) (see attached map). *Dusty dry ice unit* (DD) is related to spectrum D, which is the endmember of the green class in the SAM product (Figs. 2-3-4 and Tab. 3). This unit seems to be associated with purplish layers in the BDI1000VIS_BD15002_BD1435 and RBR_BD15002_BD1435 RGBs. This means that it should be composed of dry ice mixed with Fe-bearing dust. Its albedo in HiRISE and CTX images is higher than that of the dry ice unit and appears reddish in TRU image (Fig. 6a). Respective subunits are *dusty dry ice 3* (DD3), *dusty dry ice 4* (DD4), *dusty dry ice 5* (DD5), *dusty dry ice 6* (DD6). In optical

images, only dusty dry ice 4 (DD4) shows a well-defined stratified sequence of light and dark materials, instead all the other subunits display an irregular alternation of layers. Spectrum C, which allowed the sea green class to be distinguished in the SAM product (Figs. 2-3-4 and Tab. 3), displays an irregular alternation of layers, but bright strata are less numerous and less brilliant than those of spectrum E possibly because of a higher amount of dust with respect to the layers beneath. This is why we named the relative subunits *dark dusty dry ice 1* (DD1) and *dark dusty dry ice 2* (DD2), as part of dusty dry ice unit (see attached map).

Undifferentiated ice-dominated bedrock

We identified the unit *undifferentiated ice-dominated bedrock* (UB) wherever aeolian sediments heavily cover the stratifications precluding the identification of potential differentiation within the North Polar Layered Deposits underneath.

Surficial units

The katabatic winds blow in a direction orthogonal to the elongation of the valley eroding downslope on the south facing scarp and depositing in the north facing slope (Massé et al., 2012). In this scarp we identified some aeolian units, which are dominated by dusty or pure ice. We distinguished these units on the basis of the point of accumulation of the sediments (Fig. 6c-d and attached map): *aeolian mantling deposits* (ad) and *floor-valley deposits* (vd), which are characterised by a mixture of dust and dry ice.

Gravitational mass movements and deposits (gd) are three different landslide events that involve materials with different composition. This kind of movements usually form during summer season as a consequence of the sublimation of interstitial ice. Indeed, they are more evident in the summer CTX (Fig.6c-d and attached map).

Finally, along the north-facing scarp we identified *scarp talus deposits* (td), a unit derived by wind erosion and gravitational deposits covered by aeolian mantle of dusty dry ice.

In our geological map, all these units have transparent background with different filling pattern depending on their genesis and classification.

Stratigraphic column and geological sections

The relationships of our stratigraphy with the one from the literature is shown in the attached map and Tab.3 where the water ice unit (WI) corresponds to Planum Boreum 3 unit of Tanaka et al. (2008) and all the other belong to Planum Boreum 1; in addition, all of them are contained in Putzig et al. (2009) unit G.

As explained in Section “Methods”, the cross-sections were produced using the integration of the geologic limits in the geological map with the radargrams. Variations of dielectric constant among strata depend on the presence of almost pure water ice in the surficial layers and the increase of dry ice content in the deeper ones, as well as the different amount of dust affects the signal of the radar reflectance, which is stronger for water-ice layers, weaker for dry ice and particularly low in case of high content of dust (Putzig et al., 2009; Lauro et al., 2012). Our geological unit boundaries match with the radar reflector layers being the water unit (WI) and dusty water ice (WD) more reflective than the dry ice unit (DI) and the dusty dry ice unit (DD), which is the darkest among all the units. The color of each contact within the geological sections is referred to the unit on the top (Fig.7). Solid lines indicate boundaries separating map-derived subunits: among them are dusty water ice top (WD1), dusty dry ice 1 (DD1) or dry ice 2 (DI2) subunits. Dashed lines instead symbolize layers inferred only in the radargrams and not distinguishable in the geological map (e.g., boundary of dusty water ice top (WD1), dry ice 5 (DI5) and dusty dry ice 6 (DD6) subunits). All the cross-sections reveal subhorizontal parallel layers. Layers seem to be slightly tilted upward toward the polar dome center with an angle that increases with the depth. In particular, water-rich units show a horizontal layering and a considerable thickness (in total >100 m), while the thin CO₂-rich strata gently dip northward.

CONCLUSIONS

The Martian North Polar Cap is one of the focuses of the present-day planetary research because it can give precious information about the climate of Mars and its history (e.g., amount of dust or ice in the layers, chemical and physical processes of layer formation, effects on layer deposition due to variations of orbital parameters; Thomas et al., 2019). In this paper, we provide a highly detailed stratigraphic map of a trough facing Olympia Planum, identifying twenty-two subunits grouped into four main units plus two different kinds of deposits including aeolian and gravitational ones. The stratigraphic sequence is composed of water ice, dry ice and dust in diverse amount. Our observations confirm that water ice dominates near the surface, whereas dry ice increases with depth. This agrees with the radargram showing higher radar reflectance in the upper part of the sequence and a decrease in the deeper part (e.g., Putzig et al., 2009). This general trend is also modulated by variable dust content. Indeed, pure icy layers alternate with icy layers with variable small amount of feric minerals dust, which composition needs an in-depth spectral analysis.

Their thickness, composition and periodicity might depend on sedimentation rates, which are directly correlated with fluctuation of astronomical parameters and have controlled the past climate of Mars (Phillips et al., 2008; Becerra et al., 2017).

For the first time, we were able to identify and map variations in a stratified series at the scale of a nearly single layer through (<10 m) spectral definition thanks to a multi-instrument high-resolution survey which allowed us to project the exposed stratigraphic sequence into the subsurface.

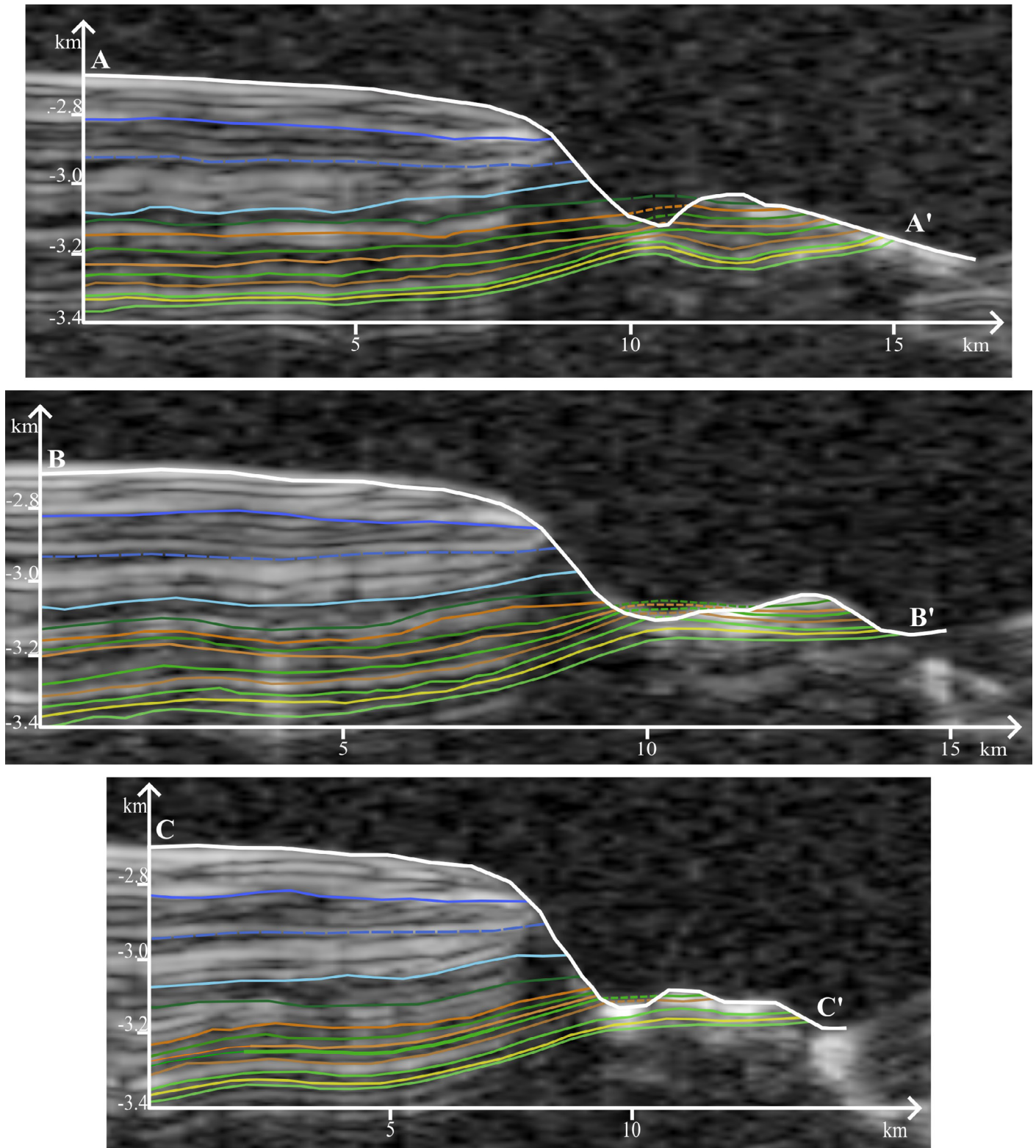


Fig. 7 - Correlation between geological units and radar reflectors. The colors of the units here are the same of the ones in the geological map. The section tracks are shown in the attached map.

Table 4 - Acronyms and related full names included in this work.

Acronym	Full name	Acronym	Full name
NASA	National Aeronautics and Space Administration	RGB	Red-Green-Blue image
CTX	Context Camera	TRU	RGB image using R600, R530 and R440 indexes
HiRISE	High Resolution Imaging Science Experiment	ICE	RGB image using BD1900_2, BD1500_2 and BD1435 indexes
CRISM	Compact Reconnaissance Imaging Spectrometer for Mars	BDI1000VIS_BD15002_BD1435	RGB image using BDI1000VIS, BD1500_2 and BD1435 indexes
SHARAD	Shallow Radar	RBR_ BD15002_BD1435	RGB image using RBR, BD1500_2 and BD1435 indexes
OMEGA	Mars Express Observatoire pour la Minéralogie, l'Eau, les Glaces et l'Activité	NPLD	North Polar Layered Deposits
THEMIS	Thermal Emission Imaging System	BU	Basal Unit
MOC	Mars Orbiter Camera	VBF	Vastitas Borealis Formation
MOLA	Mars Orbiter Laser Altimeter	WI	water ice unit
ODE	PDS Geosciences Node Mars Orbital Data Explorer	WD	dusty water ice unit
DEM	Digital Elevation Model	DD	dusty dry ice unit
QGIS	Geographic Information System software	DI	dry ice unit
Mappy	QGIS plugin for geological map generation	UB	undifferentiated ice-bedrock unit
ENVI	Geospatial Image Analysis Software	ad	aeolian mantling deposits unit
CAT	CRISM Analysis Toolkit	vd	floor-valley deposits unit
SAM	Spectral Angle Mapper classification	gd	gravitational mass movements and deposits unit
ROI	Region of Interest	td	scarp talus deposits unit
BD	Band Depth		

Indeed, several units recognised in visual images at the surface are well visible in the radargrams, we were thus able to associate the layers spectral characteristics to the radar reflectors, and so understand better the stratigraphy inside the polar body. Further work will include the replication of the same analytical process on different sites allowing the analysis of a detailed stratigraphic correlation throughout a wide region of, if not the whole, polar cap.

ACKNOWLEDGMENTS

The authors thank the reviewers and editors for the support and contributions to this scientific paper. We also acknowledge support from the EU's H2020 research and innovation program GMAP under grant agreement N° 871149, funded by EU Horizon 2020. No potential conflict of interest was reported by the authors. All data are publicly available from <https://ode.rsl.wustl.edu/mars/> and are credited to the NASA Planetary Data System (PDS).

REFERENCES

- Becerra P., Sori M.M., Byrne S. (2017) - Signals of Astronomical Climate Forcing in the Exposure Topography of the North Polar Layered Deposits of Mars. *Geophys. Res. Lett.*, 44 (1), 62-70, <https://doi.org/10.1002/2016GL071197>.
- Bultel B., Quantin C., Andreani M., Clenet H. (2013) - A New CRISM Data Analysis Tool for the Detection of Miscellaneous Alteration Phases. *EPSC Abstracts*, 8, 654, <https://meetingorganizer.copernicus.org/EPSC2013/EPSC2013-654.pdf>.
- Byrne S. (2009) - The Polar Deposits of Mars. *Annu. Rev. Earth Planet. Sci.*, 37(1), 535-560, <https://doi.org/10.1146/annurev.earth.031208.100101>.
- Clark R.N. (1999) - Spectroscopy of Rocks and Minerals, and Principles of Spectroscopy. In: Rencz, A.N. (Ed.), *Manual of Remote Sensing*, Volume 3, Remote Sensing for the Earth Sciences, John Wiley and Sons, New York, 3-58. https://www.ugpti.org/smartse/research/citations/downloads/Clark-Manual_Spectroscopy_Rocks_Minerals_Book-1999.pdf.
- Clark R.N. and Roush L. (1984) - Reflectance Spectroscopy Quantitative Analysis Techniques for Remote Sensing Applications. *J. Geophys. Res.*, 89, 6329-6340, <http://dx.doi.org/10.1029/JB089iB07p06329>.
- Carter J., Poulet F., Murchie S., Bibring J.P. (2012) - Automated processing of planetary hyperspectral datasets for the extraction of weak mineral signatures and applications to CRISM observations of hydrated silicates on Mars. *Planet. Space Sci.*, 76, 53-67, <https://doi.org/10.1016/j.pss.2012.11.007>.
- Huang R., Lin C.T., Sun W., Ding X., Zhan W., Zhu J. (2017) - The Production of Iron Oxide during Peridotite Serpentinization: Influence of Pyroxene. *Geosci. Front.*, 8(6), 1311-1321, <https://doi.org/10.1016/j.gsf.2017.01.001>.
- Kruse FA., Lefkoff A.B., Boardman J.W., Heidebrecht K.B., Shapiro A.T., Barloon P.J., Goetz A. F.H. (1993) - The Spectral Image Processing System (SIPS)-Interactive Visualization and Analysis of Imaging Spectrometer Data. *Remote Sens Environ.*, 44(2), 145-163, [https://doi.org/10.1016/0034-4257\(93\)90013-N](https://doi.org/10.1016/0034-4257(93)90013-N).
- Lauro S., Mattei E., Soldovieri F., Pettinelli E., Orosei R., Vannaroni G. (2012) - Dielectric constant estimation of the uppermost Basal Unit layer in the martian Boreales Scopuli region. *Icarus*, 219(1), 458-467, <https://doi.org/10.1016/j.icarus.2012.03.011>.
- Luo J., Ying k., Bai J. (2005) - Savitzky–Golay smoothing and differentiation filter for even number data. *Signal Processing*, 85, 1429-1434, <https://doi.org/10.1016/j.sigpro.2005.02.002>.
- Malin M.C., Bell J.F., Cantor B.A., Caplinger M.A., Calvin W.M., Clancy R.T., Edgett K.S., Edwards L., Haberle R.M., James P.B., Lee S.W., Ravine M.A., Thomas P.C., Wolff M.J. (2007) - Context Camera Investigation on Board the Mars Reconnaissance Orbiter. *J. Geophys. Res.-Planet.*, 112(5), 1-25, <https://doi.org/10.1029/2006JE002808>.
- Massé M., Bourgeois O., le Mouelic S., Verpoorter C., Spiga A., le Deit L. (2012) - Wide Distribution and Glacial Origin of Polar Gypsum on Mars. *Earth Planet. Sci. Lett.*, 317, 44-55, <https://doi.org/10.1016/j.epsl.2011.11.035>.
- McEwen A.S., Eliason E.M., Bergstrom J.W., Bridges N.T., Hansen C.J., Delamere W.A., Grant J.A., Gulick V.C., Herkenhoff K.E., Keszthelyi L., Kirk R. L., Mellon M.T., Squyres S.W., Thomas N., Weitz C.M. (2007) - Mars Reconnaissance Orbiter's High Resolution Imaging Science Experiment (HiRISE). *J. Geophys. Res.-Planet.*, 112(E5), 1-40, <https://doi.org/10.1029/2005JE002605>.
- Milkovich S.M., Head J.W. III, Neukum G. (2008) - Stratigraphic Analysis of the Northern Polar Layered Deposits of Mars: Implications for Recent Climate History. *Planet. Space Sci.*, 56(2), 266-288, <https://doi.org/10.1016/j.pss.2007.08.004>.
- Mirino M., Sefton-Nash E., Witasse O., Frigeri A., Holt J.W., Nerozzi S. (2018) - Multi-instrument data handling for sub-surface analysis on Mars. In: 49th Lunar and Planetary Science Conference, March 19-23, 2018, Woodlands (Texas-USA), Contribution. No. 2083, <https://www.hou.usra.edu/meetings/lpsc2018/pdf/2281.pdf>.
- Murchie S., Arvidson R., Bedini P., Beisser K., Bibring J.-P., Bishop J., Boldt J., Cavender P., Choo T., Clancy R.T., Darlington E.H., Des Marais D., Espiritu R., Fort D., Green R., Guinness E., Hayes J., Hash C., Heffernan K., Hemmler J., Heyler G., Humm D., Hutcheson J., Izenberg N., Lee R., Lees J., Lohr D., Malaret E., Martin T., McGovern J.A., McGuire P., Morris R., Mustard J., Pelkey S., Rhodes E., Robinson M., Roush T., Schaefer E., Seagrave G., Seelos F., Silverglate P., S. Slavney S., Smith M., Shyong W.-J., Strohhahn K., Taylor H., Thompson P., Tossman B., Wirzburger M., Wolff M. (2007) - Compact Reconnaissance Imaging Spectrometer for Mars (CRISM) on Mars Reconnaissance Orbiter (MRO). *J. Geophys. Res.-Planet.*, 112(5), 1-57, <https://doi.org/10.1029/2006JE002682>.
- Ojha L., Nerozzi S., Lewis K. (2019) - Compositional Constraints on the North Polar Cap of Mars from Gravity and Topography. *Geophys. Res. Lett.*, 46(15), 8671-8679, <https://doi.org/10.1029/2019GL082294>.
- Penasa L., Frigeri A., Pozzobon R., Brandt C.H., De Toffoli B., Naß A., Rossi A.P., Massironi M. (2020) - Constructing and deconstructing geological maps: a QGIS plugin for creating topologically consistent geological cartography. *Europlanet Science Congress 2020 (EPSC)*, 14, EPSC2020-1057, <https://doi.org/10.5194/epsc2020-1057>.
- Phillips R.J., Zuber M.T., Smrekar S.E., Mellon M.T., Head J.W., Tanaka K.L., Putzig N.E., Milkovich S.M., Campbell B.A., Plaut J.J., Safaeinili A., Seu R., Biccari D., Carter L.M., Picardi G., Orosei R., Mohit P.S., Heggy E., Zurek R.W., Egan A.F., Giacomoni E., Russo F., Cutigni M., Pettinelli E., Holt J.W., Leuschen C.J., Marinangeli L. (2008) - Mars North Polar Deposits: Stratigraphy, Age, and Geodynamical Response. *Science*, 320(5880), 1182-1185, <https://doi.org/10.1126/science.1157546>.
- Putzig N.E., Phillips R.J., Campbell B.A., Holt J.W., Plaut J.J., Carter L.M., Egan A.F., Bernardini F., Safaeinili A., Seu R. (2009) - Subsurface Structure of Planum Boreum from Mars Reconnaissance Orbiter Shallow Radar Soundings. *Icarus*, 204(2), 443-457, <https://doi.org/10.1016/j.icarus.2009.07.034>.
- Seelos K.D., Viviano C.E., Ackiss S.E., Kremer C.H., Murchie S.L. (2019) - The MICA FILES: a compilation and reference document for minerals identified through CRISM analysis. 50th Lunar and Planetary Science Conference 2019, LPI Contribution No. 2132, id.2745, <https://www.hou.usra.edu/meetings/lpsc2019/pdf/2745.pdf>.

- Seu R., Phillips R.J., Biccari D., Orosei R., Masdea A., Picardi G., Safaeinili A., Campbell B.A., Plaut J.J., Marinangeli L., Smrekar S.E., Nunes D.C. (2007) - SHARAD sounding radar on the Mars Reconnaissance Orbiter. *J. Geophys. Res.-Planet.*, 112(E5), 1-18, <https://doi.org/10.1029/2006JE002745>.
- Skinner J.A. Jr, Herkenhoff K.E. (2012) - Geologic map of the MTM 85200 quadrangle, Olympia Rupēs region of Mars: U.S. Geological Survey Scientific Investigations Map 3197, pamphlet 12 p., 1 sheet, scale 1:500000, <https://pubs.usgs.gov/sim/3197/>.
- Smith D.E., Zuber M.T., Frey H.V., Garvin J.B., Head J.W., Muhleman D.O., Pettengill G.H., Phillips R.J., Solomon S.C., Zwally H.J., Banerdt W.B., Duxbury T.C., Golombek M.P., Lemoine F.G., Neumann G.A., Rowlands D.D., Aharonson O., Ford P.G., Ivanov A.B., Johnson C.L., McGovern P.J., Abshire J.B., Afzal R.S., Xiaoli S. (2001) - Mars Orbiter Laser Altimeter: Experiment Summary after the First Year of Global Mapping of Mars. *J. Geophys. Res.-Planet.*, 106(E10), 23689-23722, <https://doi.org/10.1029/2000JE001364>.
- Tanaka K.L., Rodriguez J.A.P., Skinner J.A. Jr., Bourke M.C., Fortezzo C.M., Herkenhoff K.E., Kolb E.J., Okubo C.H. (2008) - North Polar Region of Mars: Advances in Stratigraphy, Structure, and Erosional Modification. *Icarus*, 196(2), 318-358, <https://doi.org/10.1016/j.icarus.2008.01.021>.
- Thomas N., Becerra P., Smith I.B. (2022) - Mars and the Science Programme - the case for Mars Polar Science. *Exp. Astron.*, 54, 677-693, <https://doi.org/10.1007/s10686-021-09760-6>.
- Viviano-Beck C.E., Seelos F.P., Murchie S.L., Kahn E.G., Seelos, Taylor H.W., Taylor K., Ehlmann B.L., Wiseman S.M., Mustard J.F., Morgan M.F. (2014) - Revised CRISM Spectral Parameters and Summary Products Based on the Currently Detected Mineral Diversity on Mars. *J. Geophys. Res.-Planet.*, 119(6), 1403-1431, <https://doi.org/10.1002/2014JE004627>.
- Weber I., Böttger U., Hanke F., Reitze M. P., Heeger M., Adolphs T. & Arlinghaus H. F. (2022) - Space weathering simulation of micrometeorite bombardment on silicates and their mixture for space application. *J. Raman Spectrosc.*, 53(3), 411-419, <https://doi.org/10.1002/jrs.6162>.
- Zuber M.T., Smith D.E. (1998) - Observations of the North Polar Region of Mars from the Mars Orbiter Laser Altimeter. *Science*, 282(5396), 2053-2060, <https://doi.org/10.1126/science.282.5396.2053>.
- Zuber M.T., Smith D.E., Solomon S.C., Abshire J.B., Afzal R.S., Aharonson O., Fishbaugh K., Ford P.G., Frey H.V., Garvin J.B., Head J.W., Ivanov A.I., Johnson C.L., Muhleman D.O., Neumann G.A., Pettengill G.H., Phillips R.J., Sun X., Zwally H.J., Banerdt W.B., Duxbury T.C. (2007) - An Overview of the Mars Reconnaissance Orbiter (MRO) Science Mission. *J. Geophys. Res.-Planet.*, 112(5), 1-22, <https://doi.org/10.1029/2006JE002701>.

Manuscript received 29 August 2023; accepted 6 December 2023; published online 15 March 2024; editorial responsibility and handling by M. Pantalonì.